

https://dspace.org/

Exploration of the structure and interactions of 4dimethylamino3methylphenyl Nmethylcarbamate Aminocarb

Oluwatoyin Akerele; Andreas Lemmerer

WILEY-BLACKWELL
https://hdl.handle.net/10539/46660
WOS

Downloaded from a DSpace repository. https://dspace.org/

Check for updates

Acta Cryst C STRUCTURAL CHEMISTRY

ISSN 2053-2296

Exploration of the structure and interactions of 4-(dimethylamino)-3-methylphenyl *N*-methylcarbamate (Aminocarb)

Oluwatoyin Akerele* and Andreas Lemmerer*

Jan Boeyens Structural Chemistry Laboratory, Molecular Sciences Institute, School of Chemistry, University of the Witwatersrand, Private Bag 3, Johannesburg, 2050, South Africa. *Correspondence e-mail: oluwatoyin.akerele@wits.ac.za, andreas.lemmerer@wits.ac.za

Received 24 February 2025
Accepted 26 April 2025

Edited by R. I. Cooper, University of Oxford, United Kingdom

Keywords: crystal structure; noncovalent interactions; density functional theory; DFT; Aminocarb; synthetic pesticide.

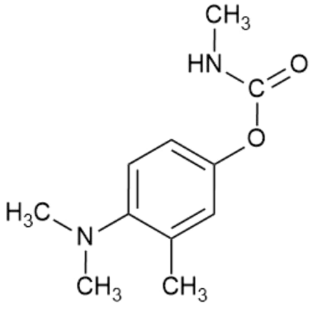
CCDC reference: 2416073

Supporting information: this article has supporting information at journals.iucr.org/c

Aminocarb [4-(dimethylamino)-3-methylphenyl *N*-methylcarbamate, $C_{11}H_{16}N_2O_2$], a synthetic pesticide, was crystallized and characterized by single-crystal and powder X-ray diffraction. In the solid state, the molecules have a strong chain N—H···O hydrogen bond with a strength of −29.37 kJ mol^{-1} and a short C—H···π contact that build a wave-like three-dimensional structure. The structural stability and intermolecular interaction of Aminocarb were investigated using differential scanning calorimetry (DSC) and density functional theory (DFT). The results show that the compound is chemically stable, and the two dominating interactions are electrostatic and dispersion energies. An electrostatic potential map reveals the binding sites of the molecules for reactivity. The understanding of the structural stability and interactions in Aminocarb provided in this study could be used to design new compounds with improved solubility and bioavailability. The dimethylamino group and the methyl group on the carbamate could be modified with other alkyl groups, which might reduce the Aminocarb toxicity, thereby leading to the development of safe, efficient and cost-effective compounds.

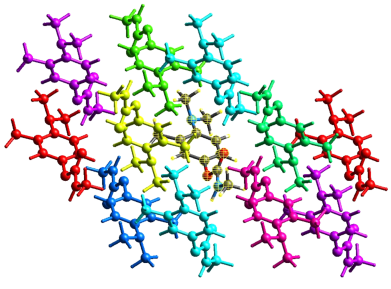
1. Introduction

Aminocarb is a synthetic pesticide in the class of carbamates (Scheme 1). It is one of the most common classes of carbamate that are commonly used for pest control of lepidopterous larvae, aphids, soil mollusks and other types of chewing insects. However, it is highly toxic to humans, animals and the environment (Moreira *et al.*, 2024; Dias *et al.*, 2014).



Aminocarb
Scheme 1

The structure of a molecule and the interactions in the solid state are related to the properties of the compound. Therefore, insight into the structural characteristics of a compound could facilitate the modification of such a compound for optimal functionality and the elimination of toxicity. In fact, an understanding of the structural properties of a compound is



OPEN ACCESS
Published under a CC BY 4.0 licence

important and has been used in different fields, including materials science, pharmaceuticals and agrochemicals (Choi, 2024; Biswas *et al.*, 2022), to improve the performance, solubility, bioavailability and stability properties of the material.

Studies have analysed the crystal structure of carbamates to understand the chemical structures and properties (Xu *et al.*, 2005; Wu *et al.*, 2009; Xia, 2010), for instance, analysis of the ethyl carbamate crystal structure provides insight into the geometry, noncovalent interactions and packing arrangements in the solid state (Bamigboye *et al.*, 2021). Similarly, the crystal structure of the inner salt of 2-[(aminoiminomethyl)amino]-ethylcarbamic acid and its analysis highlighted the geometry and interactions in the compound (Matulková *et al.*, 2017). However, there is no study on the analysis of the crystal structure and properties of Aminocarb in the literature.

In this article, we will analyse the crystal structure of Aminocarb and its interactions to provide insight into the geometry, bonding, packing arrangement and stability of the structure in the solid state. Insecticides with better chemical stability last longer and are more effective in controlling pests and disease vectors. The insight from this study could facilitate the development of effective, safe and less toxic analogues of Aminocarb, thereby reducing the environmental pollution of the compound.

2. Materials and methods

2.1. Experimental

2.1.1. Crystal growth experiment

High-purity Aminocarb was purchased from Sigma–Aldrich and utilized as received. Aminocarb (10 mg) was dissolved in acetone (2 ml). The solution was heated and stirred gently on a hotplate at a low temperature of about 30 °C until the compound dissolved completely. The heated solution was cooled to room temperature, before the vial was covered with a perforated Parafilm sheet to allow for the slow evaporation of the solvent. Prismatic crystals formed after 3 d and a suitably sized crystal was carefully selected for single-crystal X-ray diffraction (SCXRD) to ascertain the crystal structure.

2.1.2. Refinement

Crystal data, data collection and structure refinement details are summarized in Table 1. All atoms were refined anisotropically before the inclusion of H atoms. C-bound H atoms on aromatic rings were placed in calculated positions, and the sp^3-hybridized C-bound H atoms were placed in calculated positions that match the electron-density map. The N-bound H atom was located in the difference Fourier map, and its fractional coordinates and isotropic displacement parameter refined freely.

2.1.3. Powder X-ray diffraction (PXRD)

A diffractogram of a powdered crystalline sample of Aminocarb was measured at 293 K using a Bruker D2 phaser powder X-ray diffractometer. The instrument was equipped with a sealed-tube Co $K\alpha_1$ X-ray source (λ = 1.78896 Å) and a LynxEye PSD detector in Bragg–Brentano geometry, and operated at 30 kV and 10 mA. The data collection was carried out with a scanning interval ranging from 2θ = 5.0015 to 40° at a scan speed of 0.5 s per step (with an increment step size of 0.028445°). The *X'Pert High Score Plus* (Degen & van den Oever, 2009) software program was used to analyze the PXRD pattern, and the result was compared with the simulated pattern obtained from the SCXRD data to further establish the formation of the crystal structure.

Table 1
Experimental details.

Crystal data	
Chemical formula	$C_{11}H_{16}N_2O_2$
M_r	208.26
Crystal system, space group	Monoclinic, $P2_1/c$
Temperature (K)	173
a, b, c (Å)	9.2445 (3), 12.4193 (4), 9.9910 (4)
β (°)	98.929 (1)
V (Å^3)	1133.17 (7)
Z	4
Radiation type	Mo $K\alpha$
μ (mm^{-1})	0.09
Crystal size (mm)	0.29 × 0.28 × 0.15
Data collection	
Diffractometer	Bruker APEXII CCD
Absorption correction	Multi-scan (*SADABS*; Bruker, 2016; Krause *et al.*, 2015)
T_{min}, T_{max}	0.595, 0.746
No. of measured, independent and observed [$I > 2\sigma(I)$] reflections	20029, 2719, 2468
R_{int}	0.056
(sin $\theta/\lambda)_{max}$ (Å^{-1})	0.660
Refinement	
$R[F^2 > 2\sigma(F^2)]$, $wR(F^2)$, S	0.041, 0.118, 1.06
No. of reflections	2719
No. of parameters	145
H-atom treatment	H atoms treated by a mixture of independent and constrained refinement
$\Delta\rho_{max}$, $\Delta\rho_{min}$ (e Å^{-3})	0.34, −0.27

Computer programs: *APEX4* (Bruker, 2016), *SAINT* (Bruker, 2016), *SHELXT2018* (Sheldrick, 2015*a*), *SHELXL2018* (Sheldrick, 2015*b*), *OLEX2* (Dolomanov *et al.*, 2009) and *Mercury* (Macrae *et al.*, 2020).

2.1.4. Thermal analysis

Differential scanning calorimetry (DSC) detects the thermal changes in a material relative to a reference by measuring the change in the heat flow of a sample as temperature or time changes (Newman & Wenslow, 2018). Samples are heated and cooled to determine the melting points and enthalpies, and to detect any phase transitions. A Mettler Toledo DSC 3 was used to collect the DSC data, and aluminium pans were placed under nitrogen gas at a flow rate of 10 ml min^{-1}. The temperature and energy calibrations were performed using pure indium (purity 99.9%, m.p. 156.6 °C, heat of fusion 28.45 J g^{-1}) and pure zinc (purity 99.9%, m.p. 419.5 °C, heat of fusion 112 J g^{-1}). At a heating or cooling rate of 10 °C min^{-1}, the samples were heated from 25 to 155 °C and then cooled to 25 °C.

s2053229625003078X by South African Medical Research, Wiley Online Library on [17/09/2025]. See the Terms and Conditions (https://onlinelibrary.wiley.com/terms-and-conditions) on Wiley Online Library for rules of use; OA articles are governed by the applicable Creative Commons License

2.1.5. Cambridge Structural Database analysis

The CSD (Version 5.44; Groom *et al.*, 2016) was used to analyse the structure of Aminocarb.

2.2. Theoretical studies (using density functional theory, DFT)

2.2.1. Geometry optimization

The *GAUSSIAN16* suite of programs (Frisch *et al.*, 2016) was used for the minimization of Aminocarb with the default Berny algorithm (Li & Frisch, 2006). Geometry optimization of the Aminocarb structure obtained from the solved crystal structure was calculated in the gas phase at the M06l functional (Wang *et al.*, 2017; Zhao & Truhlar, 2008*a*) with the def2-TZVP basis set (Zhao & Truhlar, 2008*b*) and incorporate Grimme's D3 dispersion correction (Grimme *et al.*, 2010) for a proper description of the dispersion interactions. The frequency computation was additionally computed at the same theoretical level (M06l-D3/def2-TZVP) to ensure no imaginary frequency and to ascertain that the structure that was optimized is a universal minimal structure with the lowest energy. *Chemcraft* (Zhurko & Zhurko, 2015) software was used in this study to analyze and visualize the output generated from Gaussian calculations. The program extracts the relevant information and presents it in a clear way for easy understanding of the output.

2.2.2. Interaction energy of units in Aminocarb crystallized structures

The H-atom positions of two molecular structures related by an inversion symmetry operation, obtained from the crystal structures, were optimized separately in the gas phase at the same theoretical (M06l-D3/def2-TZVP) method because the H-atom positions from crystal structures are not accurately determined by X-ray crystallography. This was done to obtain the interaction energy between the units in the crystal structure of Aminocarb, and it was calculated with the same theoretical method, taking the basis set superposition error (BSSE) into account with the counterpoise correction (Simon *et al.*, 1996; Boys & Bernardi, 1970; Ransil, 1961). The expression for the interaction energy is given by

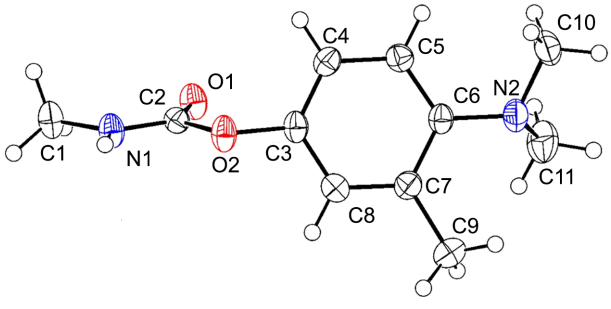


Figure 1
The molecular structure and asymmetric unit of Aminocarb, with displacement ellipsoids drawn at the 50% probability level and H atoms shown as small spheres of arbitrary radii.

$$\Delta E_{cp} = E(A)_{ab} + E(B)_{ab} - \left(E(A)_a + E(B)_b\right)$$

where ΔE_{cp} is the energy of complexation, $E(A)_{ab}$ is the energy of A calculated in the presence of B ghost basis functions, similar to $E(B)_{ab}$, $E(A)_a$ is the energy of A and $E(A)_b$ is the energy of B. The interaction energy is

$$\Delta E = E(AB)_{ab} - \left(E(A)_a + E(B)_b\right) + \Delta E_{cp}$$

2.2.3. Hirshfeld surfaces and intermolecular interaction

CrystalExplorer (Spackman *et al.*, 2021) was used in this study to generate the Hirshfeld surfaces (HS) at high standard resolution using the CIF as the input file. *CrystalExplorer* creates colour-coded and HS surface maps that help to visualize the important regions of the intermolecular interactions on the surface. The standard normalized contact (d_{norm}) of Hirshfeld surface analysis is given as follows:

$$d_{norm} = \frac{d_i - r_i^{VDW}}{r_i^{VDW}} + \frac{d_e - r_e^{VDW}}{r_e^{VDW}}$$

where d_i is the distance that represents nearest core inside the surface and d_e is the distance from the HS to the nearest core outside the surface (Dege *et al.*, 2022).

The d_{norm} is the distances range between the surface and the nearest atomic external surfaces (d_e) and internal surfaces (d_i). Red contacts are those that are shorter than van der Waals radii (vdW), indicating that the atoms that form intermolecular bonds are closer than the sum of their radii (Spackman *et al.*, 2008). Contacts with distances equal to the sum of the vdW radii are shown on the white surface. A blue colour indicates interactions that are more distinct – that is, contacts that are longer than the sum of the vdW radii (Dege *et al.*, 2022; Zeng *et al.*, 2023; Garg & Azim, 2022; Garg *et al.*, 2021, 2022).

CrystalExplorer was also used in this study to calculate the intermolecular interaction energies of the crystal structure. The wavefunctions of the molecular system were calculated with the built-in *TONTO* program at the CE-B3LYP/6-31G-(d,p) theoretical level (Jayatilaka & Grimwood, 2003; Mackenzie *et al.*, 2017; Turner *et al.*, 2015). All the energies of interaction between the selected molecule (at the centre of the cluster) and its neighbouring molecules were computed; the model then separated the total energies into different components such as electrostatic, polarization, dispersion and repulsion energy components.

3. Results and discussion

3.1. Experimental results

3.1.1. Single-crystal X-ray diffraction (SCXRD) results

Aminocarb crystallized in the monoclinic space group $P2_1/c$ with $Z' = 1$ (Fig. 1). Molecules of Aminocarb related by the glide-plane operation form a hydrogen-bonded chain with a $C(4)$ motif (Bernstein *et al.*, 1995), using the N1—H1···O1^{i} hydrogen bond, as shown in Fig. 2(*a*) and Table 2. Adjacent chains are connected *via* a short contact from H10*B* to the ring

s2053229625003078X by South African Medical Research, Wiley Online Library on [17/09/2025]. See the Terms and Conditions (https://onlinelibrary.wiley.com/terms-and-conditions) on Wiley Online Library for rules of use; OA articles are governed by the applicable Creative Commons License

Table 2
Hydrogen-bond geometry (Å, °).

D—H···A	D—H	H···A	D···A	D—H···A
N1—H1···O1^{i}	0.825 (17)	2.083 (17)	2.8174 (12)	148.1 (15)

Symmetry code: (i) $x, -y+\frac{3}{2}, z+\frac{1}{2}$.

centroid of an adjacent molecule [C10—H10B···π, with H10B···π = 2.90 Å; the centroid (Cg) is at (x, $-y+\frac{1}{2}$, $z-\frac{1}{2}$)]. The Aminocarb molecules form layers that stack on top of one another, giving a wave-like shape in the overall packing when viewed along the a axis, as shown Figs. 2(b) and 2(c).

3.1.2. PXRD

PXRD is an effective detection tool that can be used to ascertain phase purity in a bulk polycrystalline sample. The overlay of the powder pattern from the PXRD experiment and that simulated from the SCXRD experiment exhibit a shift in peak positions due to the different temperatures of the experiments (293 and 173 K, respectively). The PXRD data are not of sufficient quality to conclusively rule out minor impurities, but the strong diffraction peaks are observed at related d-spacings in both patterns. The PXRD result is presented in the supporting information.

3.1.3. Differential scanning calorimetry (DSC)

The DSC thermograms of Aminocarb were obtained to determine the melting point and enthalpy of fusion, and to ascertain the presence of phase changes. The thermal data as given in Fig. 3 show an onset of melting point of 94.88 °C, and the enthalpy of melting is −26.46 kJ mol^{-1}. The results indicate that Aminocarb is relatively thermally and chemically stable up to its melting point. However, the compound does not show any phase transition.

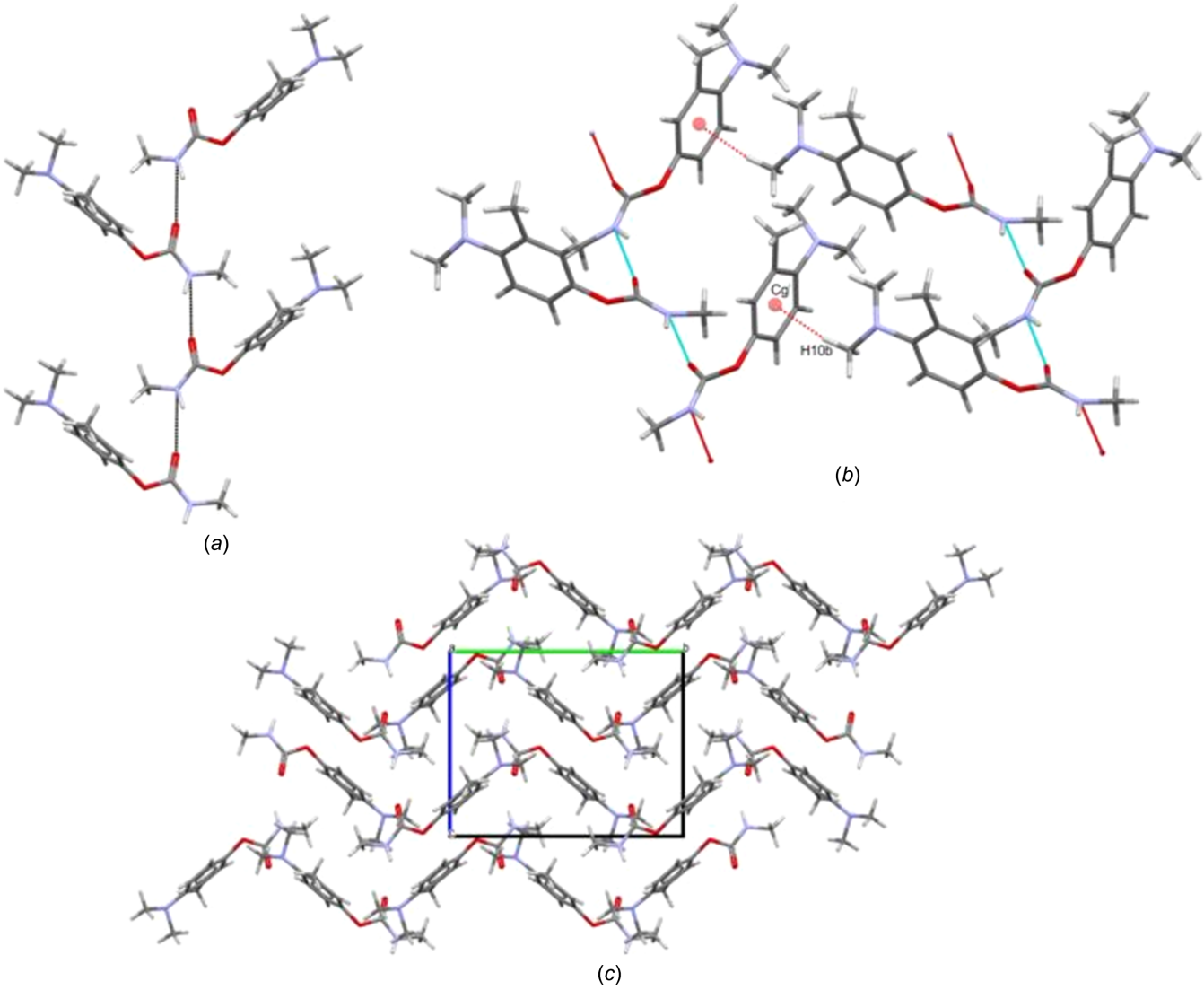


Figure 2
(a) The chain hydrogen bond $C(4)$; (b) the C—H···π contact joining adjacent chains [symmetry code: (i) $x, -y+\frac{1}{2}, z-\frac{1}{2}$]; ($c$) molecules packed in opposite directions in a wave-like manner in the overall packing.

s2053229625003078X, 2025, 6, Downloaded from https://onlinelibrary.wiley.com/doi/10.1107/S2053229625003078X by South African Medical Research, Wiley Online Library on [17/09/2025]. See the Terms and Conditions (https://onlinelibrary.wiley.com/terms-and-conditions) on Wiley Online Library for rules of use; OA articles are governed by the applicable Creative Commons License

3.2. Theoretical results

3.2.1. Full geometry optimization of the Aminocarb structure

The optimized structure of Aminocarb (Fig. 4) calculated with density functional theory (DFT) has a minimum energy value of -1.81×10^6 kJ mol^{-1}. The geometry shows excellent agreement with the X-ray data of Aminocarb.

3.2.2. Energetic properties of the structure of Aminocarb

The interaction energy between two Aminocarb structures related by a "glide plane operation is -7.02 kcal mol^{-1} (-29.37 kJ mol^{-1}) in the gas phase. This suggests that the chain hydrogen bond between two molecules of Aminocarb, as shown in Fig. 2(*a*), is quite strong and is contributing to the stability of the crystal structure.

3.2.3. Hirshfeld surface (HS) analysis of the Aminocarb structure

To visualize the molecular packing and interactions in the crystal structure, the structure HS analysis was generated using *CrystalExplorer* (Version 21) (Dege *et al.*, 2022; Spackman & Jayatilaka, 2009).

3.2.4. Fingerprint plots (FP)

The percentage contributions of the different atoms in close contact (interaction) in the crystal structure packing of Aminocarb are given in Fig. 5. The d_i and d_e distances – the former representing the distance from the HS to the nearest atom outside and the latter representing the distance from the HS to the nearest atom in the interior – are used to construct the FP (Dege *et al.*, 2022).

The 2D fingerprint plots of the structure, as well as split into individual elements, are displayed in Fig. 5. The H···H interactions account for the largest portion of the HS region in the 2D fingerprint maps, representing 62.4%. The O···H/H···O interactions account for 17.9% of the two sharp spikes. The other contacts are C···H/H···C (16.7%) and N···H/H···N (3.1%). These contacts suggest that electrostatic and dispersion interactions may be the dominant noncovalent interactions in the crystal structure.

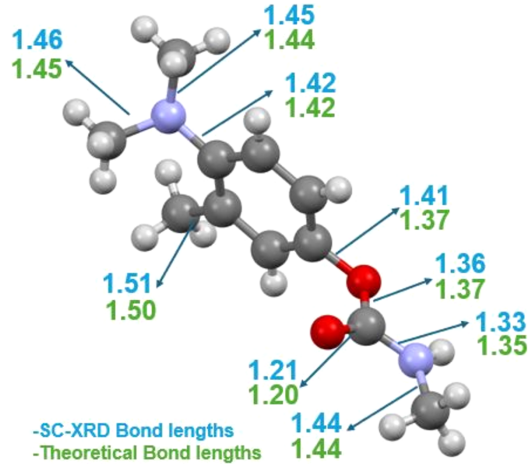


Figure 4
The geometry-optimized structure of Aminocarb. The experimental bond length is shown in sky blue, while the DFT bond length is in green (the stated values are in Ångstroms).

3.2.5. Surfaces: d_{norm}, curvedness, shape index and electrostatic potential

The colour-coded distances representing the different intermolecular interactions of the structure were mapped onto the Hirshfeld surfaces.

(1) The HS is plotted over d_{norm} in Fig. 6. The intensity of the red spots is a qualitative indicator of the strength of the contacts, as seen in the intermolecular interactions presented.

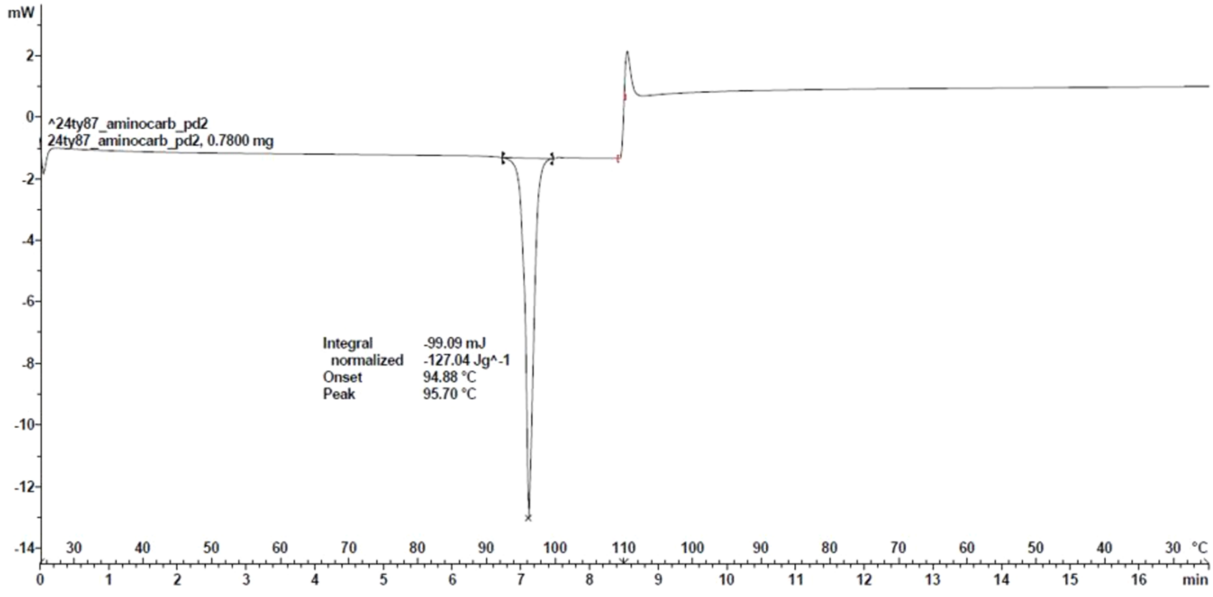
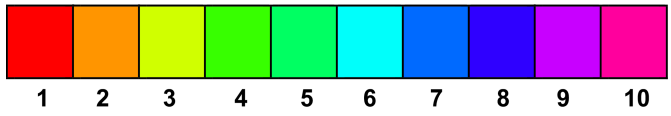


Figure 3
DSC scan of the Aminocarb structure.

s205322962, 2025, 6, Downloaded from https://onlinelibrary.wiley.com/doi/10.1107/S205322962500378X by South African Medical Research, Wiley Online Library on [17/09/2025]. See the Terms and Conditions (https://onlinelibrary.wiley.com/terms-and-conditions) on Wiley Online Library for rules of use; OA articles are governed by the applicable Creative Commons License

Table 3
The theoretical interaction energy of the Aminocarb molecule (in kJ mol^{-1}).

The total of the four energy components – polarization (E_{pol}), dispersion (E_{dis}), repulsion (E_{rep}) and electrostatic (E_{ele}) energies – is the interaction energy (E_{tot}). R is the atomic position (distance in Å) between molecular centres.



No.	N	Symop	R	Electron density	E_{ele}	E_{pol}	E_{dis}	E_{rep}	E_{tot}
1	2	x, y, z	9.24	B3LYP/6-31G(d,p)	0.2	−0.1	−1.7	0.0	−1.3
2	2	$x, -y+\frac{1}{2}, z+\frac{1}{2}$	8.20	B3LYP/6-31G(d,p)	−5.3	−0.9	−24.2	15.0	−18.1
3	2	$-x, y+\frac{1}{2}, -z+\frac{1}{2}$	7.50	B3LYP/6-31G(d,p)	−3.0	−1.3	−26.2	14.6	−17.9
4	1	$-x, -y, -z$	6.81	B3LYP/6-31G(d,p)	−4.5	−1.8	−23.7	8.6	−21.4
5	2	$-x, y+\frac{1}{2}, -z+\frac{1}{2}$	8.14	B3LYP/6-31G(d,p)	−6.7	−2.9	−16.5	10.9	−16.9
6	2	$x, -y+\frac{1}{2}, z+\frac{1}{2}$	7.74	B3LYP/6-31G(d,p)	−34.2	−8.9	−16.5	37.6	−33.8
7	1	$-x, -y, -z$	6.25	B3LYP/6-31G(d,p)	−2.8	−1.0	−14.5	3.9	−13.9
8	1	$-x, -y, -z$	5.90	B3LYP/6-31G(d,p)	−1.2	−0.9	−29.9	16.1	−18.1
9	2	$x, -y+\frac{1}{2}, z+\frac{1}{2}$	11.45	B3LYP/6-31G(d,p)	0.3	−0.0	−1.4	0.1	−0.9
10	1	$-x, -y, -z$	13.48	B3LYP/6-31G(d,p)	2.3	−0.3	−8.1	0.0	−4.9

The N—H···O hydrogen bonds produce two intense red patches, while the C—H contacts are indicated by a light-red region.

(2) A deeper understanding of molecular packing was obtained by mapping the HS over shape index and curvedness. This was used to gain insight into the weak interactions in the crystal packing configuration. There is no indication of stacking interactions between molecules of Aminocarb, as shown by the curvedness plot (Fig. 7), which does not display any flat surface area. This is in correlation with the fingerprint plot.

(3) The absence of red and blue triangles on the shape-index surface of Aminocarb shown in Fig. 8 demonstrated that the structure did not have a π–π stacking interaction, which

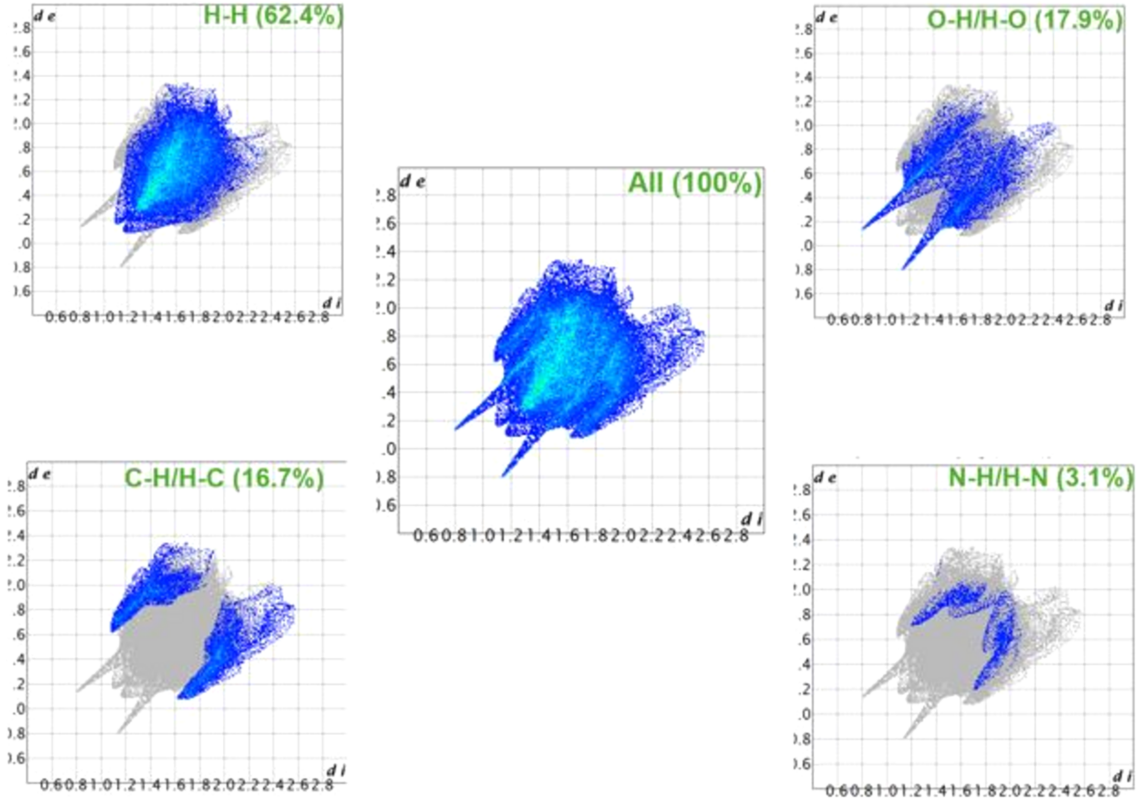


Figure 5
2D fingerprint plots of the Aminocarb structure.

s2053229625003078X by South African Medical Research, Wiley Online Library on [17/09/2025]. See the Terms and Conditions (https://onlinelibrary.wiley.com/terms-and-conditions) on Wiley Online Library for rules of use; OA articles are governed by the applicable Creative Commons License

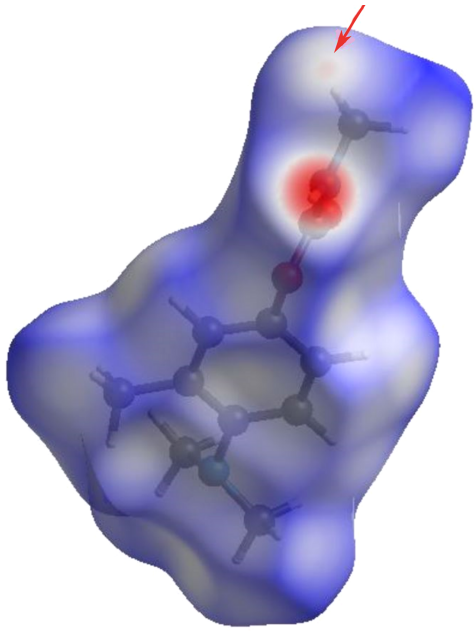


Figure 6
Three-dimensional Hirshfeld surface view along the *c* axis of Aminocarb mapped on d_{norm} between −0.5196 and 1.3010 a.u.

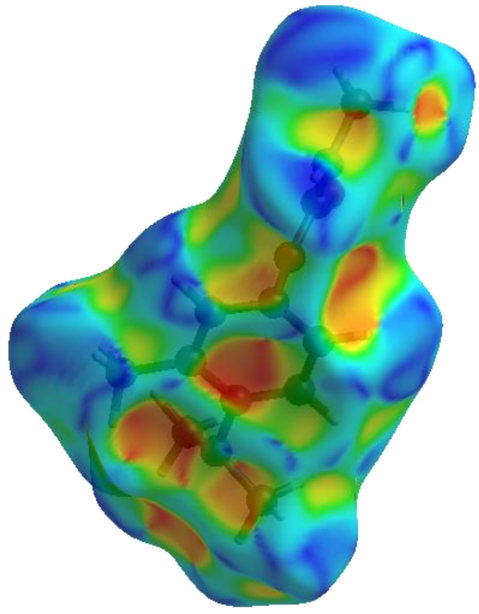


Figure 8
Three-dimensional Hirshfeld surface view along the *c* axis of Aminocarb mapped on shape index between −1.0000 and 1.0000 a.u.

supported the absence of C···C contacts in the fingerprint plot (Spackman & Jayatilaka, 2009; Garg *et al.*, 2022; Akhileshwari *et al.*, 2022).

(4) The preferred binding sites and the electron donors and acceptors were identified and visualized with the use of an electrostatic potential (ESP) map. With the B3LYP/6-311G(d, p) theoretical method, the ESP property was computed on the HS surface at high standard resolution, and the results were mapped over the computed ESP (Fig. 9) (Mackenzie *et al.*, 2017; Turner *et al.*, 2017). The areas around the atoms that correspond to electropositive and electronegative potentials are shown by blue and red, respectively, as hydrogen-bond donors and acceptors. On the ESP surface, the red region represents electrophilic sites and are electron deficient, while the blue region represents nucleophilic sites and are electron rich. In the Aminocarb structure, the negative potential is

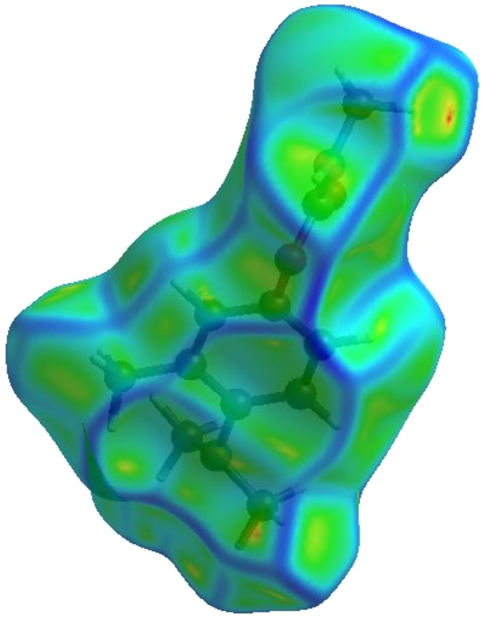


Figure 7
Three-dimensional Hirshfeld surface view along the *c* axis of Aminocarb mapped on curvedness between −4.0000 and 0.4000 a.u.

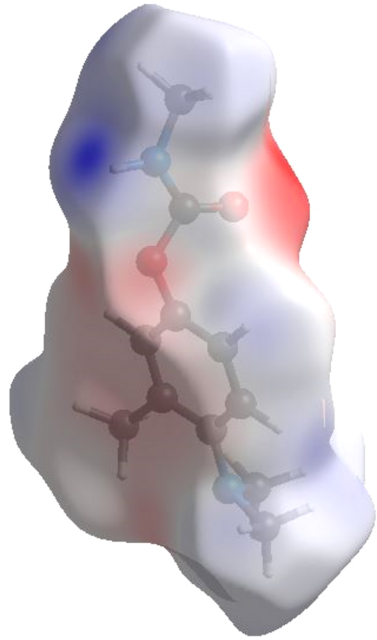


Figure 9
Three-dimensional Hirshfeld surface view of Aminocarb mapped on electrostatic potential between −0.0997 and 0.1443 a.u.

s2053229625003078X by South African Medical Research, Wiley Online Library on [17/09/2025]. See the Terms and Conditions (https://onlinelibrary.wiley.com/terms-and-conditions) on Wiley Online Library for rules of use; OA articles are governed by the applicable Creative Commons License

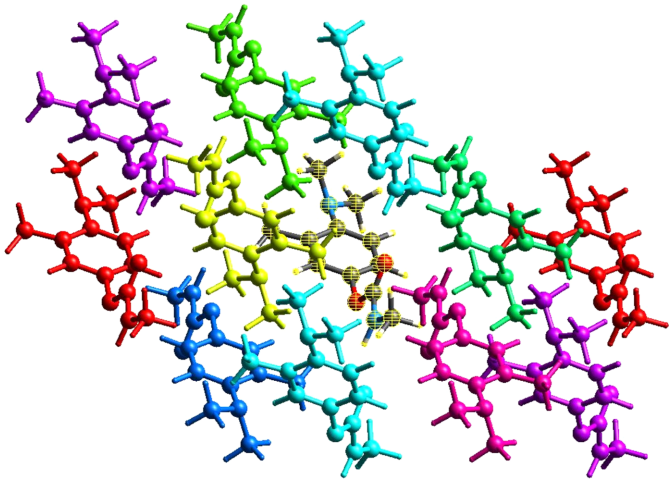


Figure 10
The Coulombic interaction, dispersion and total interaction energies of the Aminocarb molecule are shown in red, blue, purple, green, yellow and pink along the *b* axis.

around C2═O1, O2 and the C atoms in the arene ring, while the positive potential is concentrated over N1—H1 and N2.

3.2.6. Interaction energy of the crystal structure

The addition of interaction energy calculations in *CrystalExplorer* allows for the precise calculation of the intensity of interactions, which may be directly compared to the outcomes obtained from HS analysis.

The CE-B3LYP/6-31G(d,p) energy model, which is accessible in *CrystalExplorer21* (Dege *et al.*, 2022), is used to compute the intermolecular interaction energies. By default, a cluster of molecules is created by applying crystallographic symmetry operations to a chosen central molecule within a radius of 3.8 Å (Frisch *et al.*, 1984). The total energies (E_{tot}) are separated into different components, such as electrostatic (E_{ele}), polarization (E_{pol}), dispersion (E_{dis}) and repulsion (E_{rep}) energies (Hirshfeld, 1977), with their respective scale factors being 1.057, 0.740, 0.871 and 0.618 (Fig. 10).

The summation of energy of interactions (in kJ mol^{-1}) for the Aminocarb structure (Table 3) are −54.75 (E_{ele}), −11.91 (E_{pol}), −108.53 (E_{dis}), 57.17 (E_{rep}) and −118.03 (E_{tot}) for N—H···O. The evaluation of the energy components shows that the dispersion energy is the highest contributor to the stability of the structure. Electrostatic energy is also strong and contributes about half of the dispersion energy to the stability of the structure.

4. Conclusions

Aminocarb crystallized in a monoclinic crystal system and the structure packed with a characteristic wave-like pattern. The geometry of the Aminocarb structure obtained experimentally is in excellent agreement with the theoretically optimized geometry. The chain hydrogen bond in Aminocarb has an interaction energy of −29.37 kJ mol^{-1}, supporting the importance of this interaction. DSC analysis shows that the structure is chemically stable, which is in correlation with the calculated interaction energy. Reactive sites in Aminocarb are identified using a molecular electrostatic potential map. The dominant contacts in the fingerprint plot are O···H, C···H and H···H, confirming the presence of electrostatic and dispersion energy as the dominant interaction energies. The detailed information of the structural analysis, bonding, stability property and interactions energy in Aminocarb provided in this study could be used to modify the structure through functional-group manipulation to improve the properties and perhaps aid the development of safe and effective Aminocarb.

Acknowledgements

Funding for this research was provided by the School of Chemistry and a Postdoctoral grant by the URIC of the University of the Witwatersrand.

References

Akhileshwari, P., Sharanya, K. & Sridhar, M. A. (2022). *J. Chem. Crystallogr.* **52**, 324–336.
Bamigboye, C., Abbo, H. S., Kwong, H. C., Tan, S. L., Tiekink, E. R., Kamounah, F. S. & Titinchi, S. J. (2021). *Z. Kristallogr. Cryst. Mater.* **236**, 187–199.
Bernstein, J., Davis, R. E., Shimoni, L. & Chang, N. L. (1995). *Angew. Chem. Int. Ed. Engl.* **34**, 1555–1573.
Biswas, K., Gurao, N. P., Maiti, T. & Mishra, R. S. (2022). *Structural Properties*, in *High Entropy Materials: Processing, Properties, and Applications*, pp. 195–257. Singapore: Springer Nature Singapore.
Boys, S. F. & Bernardi, F. J. M. P. (1970). *Mol. Phys.* **19**, 553–566.
Bruker (2016). *APEX4* and *SAINT*. Bruker AXS Inc., Madison, Wisconsin, USA.
Choi, K. (2024). *Mini Rev. Med. Chem.* **24**, 330–340.
Dege, N., Gökce, H., Doğan, O. E., Alpaslan, G., Ağar, T., Muthu, S. & Sert, Y. (2022). *Colloids Surf. A Physicochem. Eng. Asp.* **638**, 128311.
Degen, T. & van den Oever, J. (2009). *Powder Diffr.* **24**, 163.
Dias, E., Morais, S., Ramalheira, E. & Pereira, M. L. (2014). *J. Toxicol. Environ. Health A*, **77**, 849–855.
Dolomanov, O. V., Bourhis, L. J., Gildea, R. J., Howard, J. A. K. & Puschmann, H. (2009). *J. Appl. Cryst.* **42**, 339–341.
Frisch, M. J., Pople, J. A. & Binkley, J. S. (1984). *J. Chem. Phys.* **80**, 3265–3269.
Frisch, M. J., Trucks, G. W., Schlegel, H. B., Scuseria, G. E., Robb, M. A., Cheeseman, J. R., Scalmani, G., Barone, V., Mennucci, B., Petersson, G. A., Nakatsuji, H., Caricato, M., Li, X., Hratchian, H. P., Izmaylov, A. F., Bloino, J., Zheng, G., Sonnenberg, J. L., Hada, M., Ehara, M., Toyota, K., Fukuda, R., Hasegawa, J., Ishida, M., Nakajima, T., Honda, Y., Kitao, O., Nakai, H., Vreven, T., Montgomery, J. A., Peralta, J. E., Ogliaro, F., Bearpark, M., Heyd, J. J., Brothers, E., Kudin, K. N., Staroverov, V. N., Kobayashi, R., Normand, J., Raghavachari, K., Rendell, A., Burant, J. C., Iyengar, S. S., Tomasi, J., Cossi, M., Rega, N., Millam, J. M., Klene, M., Know, J. E., Cross, J. B., Bakken, V., Adamo, C., Jaramillo, J., Gomperts, R., Stratmann, R. E., Yazyev, O. A., Austin, J., Cammi, R., Pomelli, C., Ochterski, J. O., Martin, R. L., Morokuma, K., Zakrzweski, V. G., Voth, G. A., Salvador, P., Dannenberg, J. J., Dapprich, S., Daniels, A. D., Farkas, O., Foresman, J. B., Ortiz, J. V., Cioslowski, J. & Fox, D. J. (2016). *GAUSSIAN16*. Revision C.01. Gaussian Inc., Wallingford, CT, USA. https://gaussian.com/.

s2053229625003078X by South African Medical Research, Wiley Online Library on [17/09/2025]. See the Terms and Conditions (https://onlinelibrary.wiley.com/terms-and-conditions) on Wiley Online Library for rules of use; OA articles are governed by the applicable Creative Commons License

Garg, U. & Azim, Y. (2022). *J. Mol. Struct.* **1269**, 133820.
Garg, U., Azim, Y. & Alam, M. (2021). *RSC Adv.* **11**, 21463–21474.
Garg, U., Azim, Y., Alam, M., Kar, A. & Pradeep, C. P. (2022). *Cryst. Growth Des.* **22**, 4316–4331.
Grimme, S., Antony, J., Ehrlich, S. & Krieg, H. (2010). *J. Chem. Phys.* **132**, 154104.
Groom, C. R., Bruno, I. J., Lightfoot, M. P. & Ward, S. C. (2016). *Acta Cryst.* B**72**, 171–179.
Hirshfeld, F. L. (1977). *Theor. Chim. Acta*, **44**, 129–138.
Jayatilaka, D. & Grimwood, D. J. (2003). *TONTO: a FORTRAN-based object-oriented system for quantum chemistry and crystallography*, in *International Conference on Computational Science*, pp. 142–151. Berlin, Heidelberg: Springer.
Krause, L., Herbst-Irmer, R., Sheldrick, G. M. & Stalke, D. (2015). *J. Appl. Cryst.* **48**, 3–10.
Li, X. & Frisch, M. J. (2006). *J. Chem. Theory Comput.* **2**, 835–839.
Mackenzie, C. F., Spackman, P. R., Jayatilaka, D. & Spackman, M. A. (2017). *IUCrJ*, **4**, 575–587.
Macrae, C. F., Sovago, I., Cottrell, S. J., Galek, P. T. A., McCabe, P., Pidcock, E., Platings, M., Shields, G. P., Stevens, J. S., Towler, M. & Wood, P. A. (2020). *J. Appl. Cryst.* **53**, 226–235.
Matulková, I., Charvátová, H., Císařová, I. & Štěpnička, P. (2017). *Z. Kristallogr. New Cryst. Struct.* **232**, 685–687.
Moreira, S., Martins, A. D., Alves, M. G., Pastor, L. M., Seco-Rovira, V., Oliveira, P. F. & Pereira, M. L. (2024). *Biology*, **13**, 721.
Newman, A. & Wenslow, R. (2018). *Solid-state Characterization Techniques*, in *Pharmaceutical Crystals: Science and Engineering*, edited by T. Li & A. Mattei, pp. 89–121. Hoboken, New Jersey: John Wiley & Sons Inc.
Ransil, B. J. (1961). *J. Chem. Phys.* **34**, 2109–2118.
Sheldrick, G. M. (2015*a*). *Acta Cryst.* A**71**, 3–8.
Sheldrick, G. M. (2015*b*). *Acta Cryst.* C**71**, 3–8.
Simon, S., Duran, M. & Dannenberg, J. J. (1996). *J. Chem. Phys.* **105**, 11024–11031.
Spackman, M. A. & Jayatilaka, D. (2009). *CrystEngComm*, **11**, 19–32.
Spackman, M. A., McKinnon, J. J. & Jayatilaka, D. (2008). *CrystEngComm*, **10**, 377–388.
Spackman, P. R., Turner, M. J., McKinnon, J. J., Wolff, S. K., Grimwood, D. J., Jayatilaka, D. & Spackman, M. A. (2021). *J. Appl. Cryst.* **54**, 1006–1011.
Turner, M. J., McKinnon, J. J., Wolff, S. K., Grimwood, D. J., Spackman, P. R., Jayatilaka, D. & Spackman, M. A. (2017). *CrystalExplorer17*. University of Western Australia. https://crystalexplorer.net/.
Turner, M. J., Thomas, S. P., Shi, M. W., Jayatilaka, D. & Spackman, M. A. (2015). *Chem. Commun.* **51**, 3735–3738.
Wang, Y., Jin, X., Yu, H. S., Truhlar, D. G. & He, X. (2017). *Proc. Natl Acad. Sci. USA*, **114**, 8487–8492.
Wu, J., Xie, M.-H., Luo, S.-N., Zou, P. & He, Y.-J. (2009). *Acta Cryst.* E**65**, o381.
Xia, C.-C. (2010). *Acta Cryst.* E**66**, o2580.
Xu, L.-Z., Yu, G.-P. & Yang, S.-H. (2005). *Acta Cryst.* E**61**, o1924–o1926.
Zeng, W., Wang, X., Kong, X., Li, Y. & Zhang, Y. (2023). *J. Mol. Struct.* **1279**, 135017.
Zhao, Y. & Truhlar, D. G. (2008*a*). *Acc. Chem. Res.* **41**, 157–167.
Zhao, Y. & Truhlar, D. G. (2008*b*). *Theor. Chem. Acc.* **120**, 215–241.
Zhurko, G. & Zhurko, D. (2015). *Chemcraft*. http://www.chemcraftprog.com/.

s2053229625003078X by South African Medical Research, Wiley Online Library on [17/09/2025]. See the Terms and Conditions (https://onlinelibrary.wiley.com/terms-and-conditions) on Wiley Online Library for rules of use; OA articles are governed by the applicable Creative Commons License

supporting information

Acta Cryst. (2025). C**81**, 310-318 [https://doi.org/10.1107/S205322962500378X]

Exploration of the structure and interactions of 4-(dimethylamino)-3-methylphenyl *N*-methylcarbamate (Aminocarb)

Oluwatoyin Akerele and Andreas Lemmerer

Computing details

4-(Dimethylamino)-3-methylphenyl methylcarbamate

Crystal data

$C_{11}H_{16}N_2O_2$
$M_r = 208.26$
Monoclinic, $P2_1/c$
$a = 9.2445$ (3) Å
$b = 12.4193$ (4) Å
$c = 9.9910$ (4) Å
$\beta = 98.929$ (1)°
$V = 1133.17$ (7) Å^3
$Z = 4$
$F(000) = 448$
$D_x = 1.221$ Mg m^{-3}
Mo $K\alpha$ radiation, $\lambda = 0.71073$ Å
Cell parameters from 9968 reflections
$\theta = 2.6$–$28.3°$
$\mu = 0.09$ mm^{-1}
$T = 173$ K
Prism, colourless
0.29 × 0.28 × 0.15 mm

Data collection

Bruker APEXII CCD diffractometer
φ and ω scans
Absorption correction: multi-scan (SADABS; Bruker, 2016; Krause *et al.*, 2015)
$T_{min} = 0.595$, $T_{max} = 0.746$
20029 measured reflections
2719 independent reflections
2468 reflections with $I > 2\sigma(I)$
$R_{int} = 0.056$
$\theta_{max} = 28.0°$, $\theta_{min} = 2.2°$
$h = -12 \rightarrow 12$
$k = -16 \rightarrow 16$
$l = -13 \rightarrow 13$

Refinement

Refinement on F^2
Least-squares matrix: full
$R[F^2 > 2\sigma(F^2)] = 0.041$
$wR(F^2) = 0.118$
$S = 1.06$
2719 reflections
145 parameters
0 restraints
Primary atom site location: dual
Hydrogen site location: mixed
H atoms treated by a mixture of independent and constrained refinement
$w = 1/[\sigma^2(F_o^2) + (0.0534P)^2 + 0.3083P]$ where $P = (F_o^2 + 2F_c^2)/3$
$(\Delta/\sigma)_{max} < 0.001$
$\Delta\rho_{max} = 0.34$ e Å^{-3}
$\Delta\rho_{min} = -0.27$ e Å^{-3}
Extinction correction: SHELXL2018 (Sheldrick, 2015*b*), $Fc^* = kFc[1+0.001xFc^2\lambda^3/\sin(2\theta)]^{-1/4}$
Extinction coefficient: 0.017 (4)

s205322962500378X, 2025, 6, Downloaded from https://onlinelibrary.wiley.com/doi/10.1107/S205322962500378X by South African Medical Research, Wiley Online Library on [17/09/2025]. See the Terms and Conditions (https://onlinelibrary.wiley.com/terms-and-conditions) on Wiley Online Library for rules of use; OA articles are governed by the applicable Creative Commons License

Special details

Geometry. All esds (except the esd in the dihedral angle between two l.s. planes) are estimated using the full covariance matrix. The cell esds are taken into account individually in the estimation of esds in distances, angles and torsion angles; correlations between esds in cell parameters are only used when they are defined by crystal symmetry. An approximate (isotropic) treatment of cell esds is used for estimating esds involving l.s. planes.

Refinement. Single-crystal X-ray diffraction data were obtained at 173 (2) K on a Bruker D8 Venture Bio PHOTON III 28-pixel array area detector (208 × 128 mm2) diffractometer with a Mo Kα (λ= 0.71073 Å) IμS DIAMOND source (50 kV, 1.4 mA).The APEX4 software package integrated in the instrument was used to control the experiment and analyze the diffraction data. The Bruker SAINT V8.40B (Bruker AXS Inc. Madison, WI, USA)software package in APEX4 was used to refine, reduce, and integrate the crystal data. The multi-scan method implemented in SADABS-2016 (Krause *et al.*, 2015) was used for empirical absorption corrections and correction of other systematic errors. The crystal structure was solved using intrinsic phasing (SHELXT-2018/2) (Sheldrick, 2015) and refined using SHELXL-2018/3 (Sheldrick, 2015) within the Olex2 (Dolomanov *et al.*, 2009) graphical user interface.

Fractional atomic coordinates and isotropic or equivalent isotropic displacement parameters (Å^2)

	x	*y*	*z*	U_{iso}*/U_{eq}
C1	0.94691 (15)	0.87750 (9)	0.54104 (12)	0.0383 (3)
H1A	0.925393	0.903606	0.447504	0.057*
H1B	1.053129	0.871112	0.567792	0.057*
H1C	0.907894	0.928398	0.601360	0.057*
C2	0.85428 (11)	0.70693 (8)	0.44563 (10)	0.0242 (2)
C3	0.75368 (12)	0.53609 (8)	0.38075 (10)	0.0276 (2)
C4	0.85833 (11)	0.46956 (9)	0.34131 (10)	0.0288 (2)
H4	0.959144	0.480141	0.375204	0.035*
C5	0.81382 (11)	0.38662 (8)	0.25100 (11)	0.0283 (2)
H5	0.885518	0.340819	0.222498	0.034*
C6	0.66600 (11)	0.36902 (8)	0.20112 (10)	0.0274 (2)
C7	0.56008 (12)	0.43636 (9)	0.24538 (11)	0.0307 (2)
C8	0.60681 (12)	0.52047 (9)	0.33361 (11)	0.0310 (2)
H8	0.536614	0.567796	0.361778	0.037*
C9	0.39819 (13)	0.41537 (12)	0.20829 (15)	0.0462 (3)
H9A	0.361023	0.452308	0.123207	0.069*
H9B	0.347108	0.442386	0.280403	0.069*
H9C	0.381220	0.337770	0.197136	0.069*
C10	0.72656 (15)	0.19696 (10)	0.10624 (15)	0.0433 (3)
H10A	0.806421	0.224555	0.061890	0.065*
H10B	0.679616	0.136030	0.054304	0.065*
H10C	0.765914	0.173188	0.198231	0.065*
C11	0.55224 (18)	0.31373 (13)	−0.02376 (14)	0.0530 (4)
H11A	0.484083	0.373363	−0.017912	0.080*
H11B	0.498969	0.252460	−0.069487	0.080*
H11C	0.628724	0.336801	−0.075314	0.080*
N1	0.87965 (11)	0.77349 (8)	0.55057 (9)	0.0310 (2)
N2	0.61929 (11)	0.28174 (8)	0.11263 (10)	0.0340 (2)
O1	0.88204 (9)	0.72368 (6)	0.33288 (7)	0.0330 (2)
O2	0.79138 (9)	0.61438 (6)	0.48184 (7)	0.0331 (2)
H1	0.8600 (16)	0.7530 (13)	0.6242 (17)	0.045 (4)*

s2053229625003078X, 2025, 6, Downloaded from https://onlinelibrary.wiley.com/doi/10.1107/S2053229625003078X by South African Medical Research, Wiley Online Library on [17/09/2025]. See the Terms and Conditions (https://onlinelibrary.wiley.com/terms-and-conditions) on Wiley Online Library for rules of use; OA articles are governed by the applicable Creative Commons License

Atomic displacement parameters (Å²)

	U^{11}	U^{22}	U^{33}	U^{12}	U^{13}	U^{23}
C1	0.0516 (7)	0.0303 (6)	0.0332 (6)	−0.0074 (5)	0.0077 (5)	−0.0074 (4)
C2	0.0263 (5)	0.0260 (5)	0.0200 (4)	0.0017 (3)	0.0027 (3)	0.0002 (3)
C3	0.0369 (5)	0.0254 (5)	0.0208 (5)	−0.0052 (4)	0.0054 (4)	−0.0007 (4)
C4	0.0282 (5)	0.0334 (5)	0.0247 (5)	−0.0047 (4)	0.0036 (4)	0.0006 (4)
C5	0.0299 (5)	0.0287 (5)	0.0274 (5)	−0.0008 (4)	0.0078 (4)	0.0000 (4)
C6	0.0328 (5)	0.0252 (5)	0.0245 (5)	−0.0045 (4)	0.0054 (4)	−0.0008 (4)
C7	0.0289 (5)	0.0309 (5)	0.0315 (5)	−0.0013 (4)	0.0026 (4)	−0.0009 (4)
C8	0.0327 (5)	0.0289 (5)	0.0318 (5)	0.0021 (4)	0.0065 (4)	−0.0018 (4)
C9	0.0293 (6)	0.0519 (8)	0.0559 (8)	−0.0024 (5)	0.0016 (5)	−0.0111 (6)
C10	0.0481 (7)	0.0323 (6)	0.0521 (8)	−0.0059 (5)	0.0165 (6)	−0.0140 (5)
C11	0.0635 (9)	0.0574 (9)	0.0348 (7)	−0.0054 (7)	−0.0029 (6)	−0.0123 (6)
N1	0.0444 (5)	0.0300 (5)	0.0195 (4)	−0.0050 (4)	0.0077 (4)	−0.0029 (3)
N2	0.0386 (5)	0.0309 (5)	0.0327 (5)	−0.0067 (4)	0.0063 (4)	−0.0078 (4)
O1	0.0489 (5)	0.0319 (4)	0.0196 (4)	−0.0049 (3)	0.0094 (3)	−0.0014 (3)
O2	0.0477 (5)	0.0318 (4)	0.0210 (4)	−0.0106 (3)	0.0092 (3)	−0.0039 (3)

Geometric parameters (Å, º)

C1—H1A	0.9800	C7—C8	1.3915 (15)
C1—H1B	0.9800	C7—C9	1.5076 (15)
C1—H1C	0.9800	C8—H8	0.9500
C1—N1	1.4431 (15)	C9—H9A	0.9800
C2—N1	1.3271 (13)	C9—H9B	0.9800
C2—O1	1.2116 (12)	C9—H9C	0.9800
C2—O2	1.3621 (12)	C10—H10A	0.9800
C3—C4	1.3755 (15)	C10—H10B	0.9800
C3—C8	1.3801 (16)	C10—H10C	0.9800
C3—O2	1.4063 (12)	C10—N2	1.4546 (16)
C4—H4	0.9500	C11—H11A	0.9800
C4—C5	1.3890 (15)	C11—H11B	0.9800
C5—H5	0.9500	C11—H11C	0.9800
C5—C6	1.3972 (15)	C11—N2	1.4617 (17)
C6—C7	1.4101 (15)	N1—H1	0.825 (17)
C6—N2	1.4228 (13)		
H1A—C1—H1B	109.5	C7—C8—H8	119.5
H1A—C1—H1C	109.5	C7—C9—H9A	109.5
H1B—C1—H1C	109.5	C7—C9—H9B	109.5
N1—C1—H1A	109.5	C7—C9—H9C	109.5
N1—C1—H1B	109.5	H9A—C9—H9B	109.5
N1—C1—H1C	109.5	H9A—C9—H9C	109.5
N1—C2—O2	110.25 (9)	H9B—C9—H9C	109.5
O1—C2—N1	126.20 (10)	H10A—C10—H10B	109.5
O1—C2—O2	123.55 (9)	H10A—C10—H10C	109.5
C4—C3—C8	121.08 (10)	H10B—C10—H10C	109.5

s2053229625003078X by South African Medical Research, Wiley Online Library on [17/09/2025]. See the Terms and Conditions (https://onlinelibrary.wiley.com/terms-and-conditions) on Wiley Online Library for rules of use; OA articles are governed by the applicable Creative Commons License

C4—C3—O2	120.94 (9)	N2—C10—H10A	109.5
C8—C3—O2	117.60 (9)	N2—C10—H10B	109.5
C3—C4—H4	120.6	N2—C10—H10C	109.5
C3—C4—C5	118.75 (10)	H11A—C11—H11B	109.5
C5—C4—H4	120.6	H11A—C11—H11C	109.5
C4—C5—H5	119.3	H11B—C11—H11C	109.5
C4—C5—C6	121.50 (10)	N2—C11—H11A	109.5
C6—C5—H5	119.3	N2—C11—H11B	109.5
C5—C6—C7	118.93 (9)	N2—C11—H11C	109.5
C5—C6—N2	121.77 (10)	C1—N1—H1	119.5 (11)
C7—C6—N2	119.22 (9)	C2—N1—C1	122.04 (9)
C6—C7—C9	122.11 (10)	C2—N1—H1	118.4 (11)
C8—C7—C6	118.78 (10)	C6—N2—C10	115.82 (9)
C8—C7—C9	118.96 (10)	C6—N2—C11	114.59 (10)
C3—C8—C7	120.93 (10)	C10—N2—C11	110.43 (11)
C3—C8—H8	119.5	C2—O2—C3	117.46 (8)

C3—C4—C5—C6	−0.69 (16)	C8—C3—C4—C5	0.93 (16)
C4—C3—C8—C7	0.46 (17)	C8—C3—O2—C2	−108.71 (11)
C4—C3—O2—C2	78.28 (12)	C9—C7—C8—C3	173.61 (11)
C4—C5—C6—C7	−0.90 (16)	N1—C2—O2—C3	178.34 (9)
C4—C5—C6—N2	−177.57 (10)	N2—C6—C7—C8	178.99 (10)
C5—C6—C7—C8	2.24 (16)	N2—C6—C7—C9	3.48 (17)
C5—C6—C7—C9	−173.27 (11)	O1—C2—N1—C1	−0.36 (18)
C5—C6—N2—C10	15.87 (15)	O1—C2—O2—C3	−1.78 (15)
C5—C6—N2—C11	−114.51 (13)	O2—C2—N1—C1	179.51 (10)
C6—C7—C8—C3	−2.05 (16)	O2—C3—C4—C5	173.69 (9)
C7—C6—N2—C10	−160.78 (11)	O2—C3—C8—C7	−172.54 (9)
C7—C6—N2—C11	68.84 (14)		

Hydrogen-bond geometry (Å, º)

D—H···*A*	*D*—H	H···*A*	*D*···*A*	*D*—H···*A*
N1—H1···O1^{i}	0.825 (17)	2.083 (17)	2.8174 (12)	148.1 (15)

Symmetry code: (i) *x*, −*y*+3/2, *z*+1/2.

s2053229625003078X, 2025, 6, Downloaded from https://onlinelibrary.wiley.com/doi/10.1107/S2053229625003078X by South African Medical Research, Wiley Online Library on [17/09/2025]. See the Terms and Conditions (https://onlinelibrary.wiley.com/terms-and-conditions) on Wiley Online Library for rules of use; OA articles are governed by the applicable Creative Commons License